initiated approximately 1 h after surgery. Heart rate and arterial blood pressure measurements were recorded with the aid of data acquisition software (AcqKnowledge, Biopac Systems, Inc., Goleta, CA), and end-tidal CO_2 and blood gas levels were maintained within physiologic limits.

2.2 *Image Acquisition and Analysis*

Qdot 605 amino (PEG) quantum dots (1 μM in saline, Invitrogen) were intravenously injected into the animals (1 mL/kg). To obtain a 3D structure of the cortical microvasculature, GFP-expressing RBCs and Qdot plasma were simultaneously imaged using a two-photon microscope (TCS SP5MP, Leica Microsystems, Germany) with a Ti:Sapphire laser (MaiTai HP, Spectra-Physics, CA). The excitation wavelength was 900 nm, and the emission signal was separated by a beam splitter at 560/10 nm and detected through band-pass filters of 525/50 nm and 610/75 nm for GFP and Qdot, respectively. A single image consisted of 1,024×1,024 or 512×512 pixels, and the volume image was acquired with a step size of 2.5–5 μm. For activation experiments, the right forepaw was electrically stimulated (1.5–1.7 mA, 6 Hz) [16, 17], and volume imaging was conducted before stimulation (pre-stimulus resting state) and during stimulation (activation state). The vessel diameter was compared for both RBC and plasma images.

3 Results and Discussions

The images of the microvasculature that were captured based on Qdot plasma signals showed detectable signals up to a depth of 0.6 mm from the cortical surface, which was in agreement with our previous report [3, 15]. In contrast, the images obtained with the GFP-RBC signals showed a detectable signal up to only 0.4 mm from the cortical surface. The difference in the detectable depth could be due to a differing optical property of the brain tissue for green and red wavelength ranges and/or different characteristics of the fluorescent substances themselves (GFP vs. Qdot). The quantum efficiency of Qdot is higher relative to organic dye [18], which may enhance the depth detection for Qdot plasma imaging. Based on this result, the following analysis was performed for volume images obtained up to a depth of 0.4 mm from the surface where the image contained both RBC and plasma signals.

Comparison of the vessel width showed a thicker width of Qdot plasma than that of the GFP-RBCs (Fig. 23.1). Among the vessels investigated, the plasma layer was observed to be 2–5 μm thick for venous vessels and approximately 1 μm for arterial vessels. In capillaries (<7 μm), no detectable difference in the RBC and plasma width was observed. Additionally, a variable ratio of RBC and plasma distribution was found among multiple capillaries, which indicates dynamic changes of hematocrit in single capillaries as well as among multiple capillaries. Following neural activation, the distribution of RBCs varied among the adjacent capillary networks (Fig. 23.2), which may represent the redistribution of RBCs in the activated region.

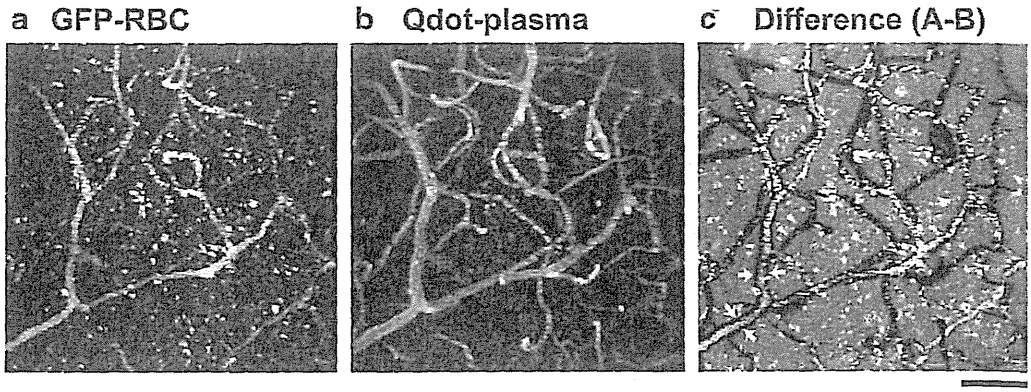

Fig. 23.1 A representative volume image of cortical microvasculature obtained with two-photon microscopy in the cerebral cortex of transgenic rats based on the fluorescent signals of GFP-RBC (**a**) and Qdot plasma (**b**). For visualization purposes, a maximum intensity projection is displayed for the images obtained over a depth of 60–200 μm from the cortical surface. (**c**) Differential image. This image was created by subtracting the plasma image (**b**) from the RBC image (**a**). The *dark area* (*arrows*) apparent in the vessel edge indicates the thicker width of the plasma (i.e., plasma layer). In contrast, no clear plasma layer was found in the capillaries (*arrow head*). The *white spots* that are seen in the extravascular area in the RBC image were due to non-GFP cells' auto-fluorescence, which has a similar emission spectrum to GFP. Scale bar: 50 μm

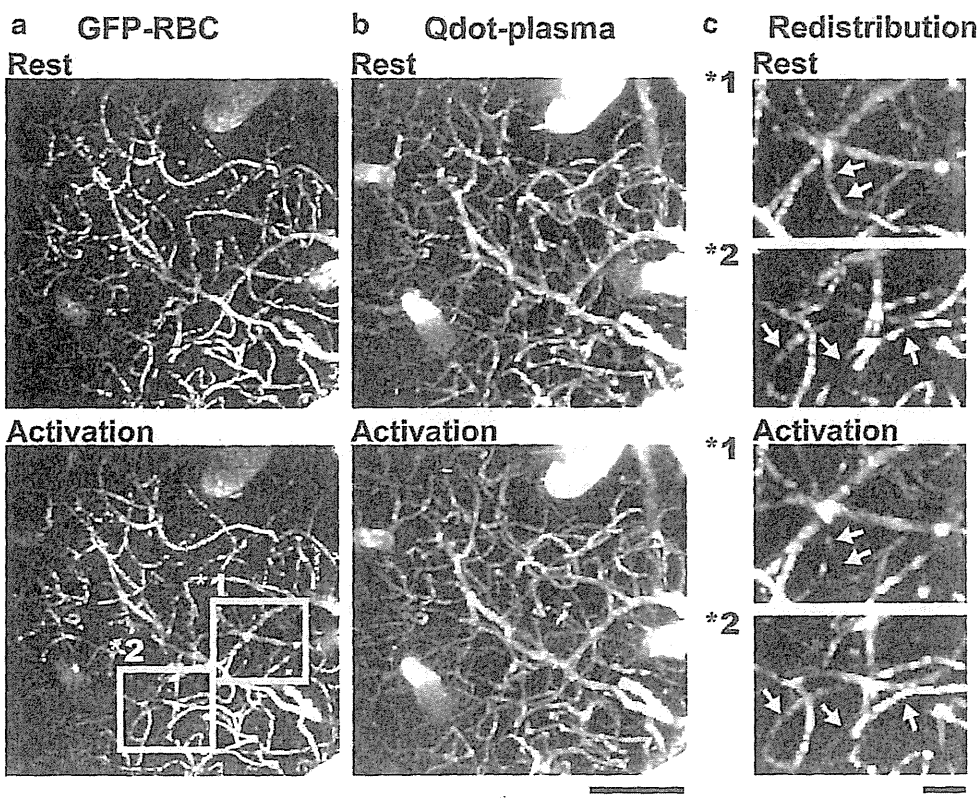

Fig. 23.2 Comparison of the cortical microvasculature during rest (*upper*) and activation (*bottom*) states. The forepaw stimulation-induced activation provoked a change of RBC (**a**) and plasma (**b**) distribution in the vessels. Scale bar: 100 μm. (**c**) Enlarged RBC image. RBC redistribution due to activation was seen in two adjacent capillary networks (regions **1* and **2*). In region **1*, RBC occupation in this capillary (*arrows*) was dense at rest but became sparse during activation. In contrast, the capillaries (*arrows*) in region *2 had increased RBC flux due to activation relative to the resting state. These observations indicate the RBC redistribution among the inter-capillaries in the adjacent capillary networks. Scale bar: 20 μm

These observations strongly indicate that there is local regulation for RBC flow at the single capillary level and/or among multiple-capillary units, which requires further investigation in relation to the activity of surrounding cells, such as neurons, astroglias, and vascular cells.

4 Summary

The present study described 3D imaging of cortical microvasculature based on GFP-expressing RBCs and Qdot-stained plasma fluorescence with two-photon microscopy. The GFP and Qdot images showed an imaging depth up to 0.4 and 0.6 mm, respectively. The plasma layer was thicker in venous vessels relative to arterial vessels of the same size. In response to neural activation, redistribution of RBC and plasma occupancy was detected in individual single capillaries and among multiple capillaries. The findings showed that the animal model presented may be useful in further investigations of the mechanism that controls RBC flow in single capillaries and multiple-capillary units in healthy and diseased brains.

Acknowledgments The authors thank Dr. Junko Taniguchi for help with the experiments. This work was partly supported by Special Coordination Funds for Promoting Science and Technology (K.M.).

References

1. Denk W, Strickler JH, Webb WW (1990) Two-photon laser scanning fluorescence microscopy. Science 248:73–76
2. Helmchen F, Denk W (2005) Deep tissue two-photon microscopy. Nat Methods 2:932–940
3. Park SH, Masamoto K, Hendrich K et al (2008) Imaging brain vasculature with BOLD microscopy: MR detection limits determined by in vivo two-photon microscopy. Magn Reson Med 59:855–865
4. Yoshihara K, Takuwa H, Kanno I et al (2012) 3D analysis of intracortical microvasculature during chronic hypoxia in mouse brain. Adv Exp Med Biol 765: 357–363
5. Kleinfeld D, Mitra PP, Helmchen F et al (1998) Fluctuations and stimulus-induced changes in blood flow observed in individual capillaries in layers 2 through 4 of rat neocortex. Proc Natl Acad Sci USA 95:15741–15746
6. Zipfel WR, Williams RM, Webb WW (2003) Nonlinear magic: multiphoton microscopy in the biosciences. Nat Biotechnol 21:1369–1377
7. Schaffer CB, Friedman B, Nishimura N et al (2006) Two-photon imaging of cortical surface microvessels reveals a robust redistribution in blood flow after vascular occlusion. PLoS Biol 4:e22
8. Dobbe JG, Streekstra GJ, Atasever B et al (2008) Measurement of functional microcirculatory geometry and velocity distributions using automated image analysis. Med Biol Eng Comput 46:659–670
9. Drew PJ, Blinder P, Cauwenberghs G et al (2010) Rapid determination of particle velocity from space-time images using the Radon transform. J Comput Neurosci 29:5–11

10. Kamoun WS, Chae SS, Lacorre DA et al (2010) Simultaneous measurement of RBC velocity, flux, hematocrit and shear rate in vascular networks. Nat Methods 7:655–660
11. Autio J, Kawaguchi H, Saito S, Aoki I, Obata T, Masamoto K, Kanno I (2011) Spatial frequency-based analysis of mean red blood cell speed in single microvessels: investigation of microvascular perfusion in rat cerebral cortex. PLoS One 6:e24056
12. Tomita M, Osada T, Schiszler I et al (2008) Automated method for tracking vast numbers of FITC-labeled RBCs in microvessels of rat brain in vivo using a high-speed confocal microscope system. Microcirculation 15:163–174
13. Unekawa M, Tomita M, Tomita Y et al (2010) RBC velocities in single capillaries of mouse and rat brains are the same, despite 10-fold difference in body size. Brain Res 1320:69–73
14. Tomita M, Tomita Y, Unekawa M et al (2011) Oscillating neuro-capillary coupling during cortical spreading depression as observed by tracking of FITC-labeled RBCs in single capillaries. Neuroimage 56:1001–1010
15. Masamoto K, Obata T, Kanno I (2010) Intracortical microcirculatory change induced by anesthesia in rat somatosensory cortex. Adv Exp Med Biol 662:57–61
16. Masamoto K, Kim T, Fukuda M et al (2007) Relationship between neural, vascular, and BOLD signals in isoflurane-anesthetized rat somatosensory cortex. Cereb Cortex 17:942–950
17. Kim T, Masamoto K, Fukuda M et al (2010) Frequency-dependent neural activity, CBF, and BOLD fMRI to somatosensory stimuli in isoflurane-anesthetized rats. Neuroimage 52: 224–233
18. Resch-Genger U, Grabolle M, Cavaliere-Jaricot S et al (2008) Quantum dots versus organic dyes as fluorescent labels. Nat Methods 5:763–775

BRAIN RESEARCH 1472 (2012) 107–112

Available online at www.sciencedirect.com

SciVerse ScienceDirect

www.elsevier.com/locate/brainres

Brain Research

Hemodynamic changes during somatosensory stimulation in awake and isoflurane-anesthetized mice measured by laser-Doppler flowmetry

Hiroyuki Takuwa[a], *Tetsuya Matsuura*[a,b], *Takayuki Obata*[a], *Hiroshi Kawaguchi*[a], *Iwao Kanno*[a], *Hiroshi Ito*[a,*]

[a]*Biophysics Program, Molecular Imaging Center, National Institute of Radiological Sciences, 4-9-1 Anagawa, Chiba 263-8555, Japan*
[b]*Academic Group of Mathematical and Natural Science, Iwate University, 4-3-5 Ueda, Morioka 020-8551, Japan*

ARTICLE INFO

Article history:
Accepted 28 June 2012
Available online 10 July 2012

Keywords:
Cerebral blood flow
Red blood cell velocity
Red blood cell concentration
Neurovascular coupling
Awake animal
Isoflurane anesthesia

ABSTRACT

Elucidating the mechanisms underlying the regulation of cerebral blood flow (CBF) is important to understanding the hemodynamic changes measured by positron emission tomography (PET) and functional magnetic resonance imaging (fMRI) signals. The purpose of this study was to explore changes in hemodynamic characteristics during resting and sensory stimulation in awake animals as compared with those in anesthetized animals. Changes in CBF, red blood cell (RBC) velocity and concentration in the somatosensory cortex to whisker stimulation were measured using laser-Doppler flowmetry in awake and anesthetized mice. The increase in the rate of RBC velocity change observed during whisker stimulation was far greater than the increase in the rate of RBC concentration change under the awake condition. During the resting condition, significant differences in baseline CBF, RBC velocity and concentration between awake and anesthesia mice were not observed. Isoflurane-induced anesthesia attenuated the increase in RBC velocity and concentration during stimulation, with the attenuation of the RBC velocity increase being greater than that of RBC concentration. The RBC measurement techniques in awake animals should lead to much better understanding of the hemodynamic system evoked by neural activity.

1. Introduction

Neural activation is accompanied by changes in regional cerebral blood flow (CBF). Although the regional hemodynamic response during neural activation can be measured by positron-emission tomography (PET) and functional magnetic resonance imaging (fMRI), the mechanisms of regional hemodynamic response during neural activation have yet not been elucidated. As a result, these mechanisms have been investigated by many researchers using anesthetized rodent models. Anesthesia significantly affects the physiological state including the regulation of cerebral circulation throughout the brain (Martin et al., 2002, 2006; Lahti et al., 1999; Peeters et al., 2001; Sicard et al., 2003; Takuwa et al., 2010). To remove the physiological effects of anesthesia, a system for an awake animal experiment for the study of brain microcirculation is needed. Thus, several studies have demonstrated measurement systems in awake rodent models using optical imaging spectroscopy, fMRI and PET (Martin et al., 2002, 2006; Sicard et al., 2003; Mizuma et al., 2010; Schulz

*Corresponding author. Fax: +81 43 206 0819.
E-mail address: hito@nirs.go.jp (H. Ito).

0006-8993/$ - see front matter © 2012 Elsevier B.V. All rights reserved.
http://dx.doi.org/10.1016/j.brainres.2012.06.049

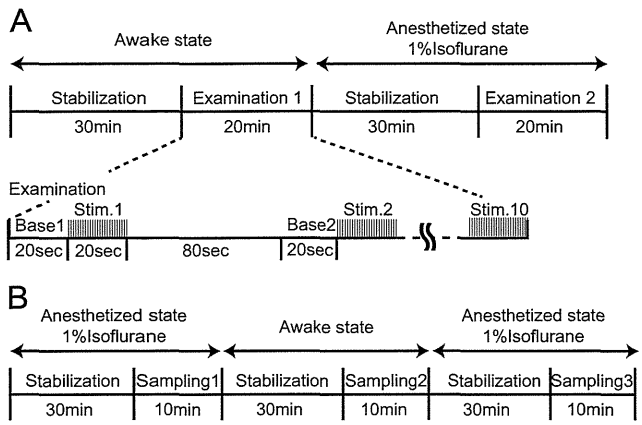

Fig. 1 – Experimental protocol for LDF measurement and blood gas sampling. (A) LDF measurements were performed in awake and anesthetized mice. Changes in CBF and RBC velocity and concentration were measured during resting state and whisker stimulation. In each examination, 10 successive stimuli (10 Hz and 20 s) were applied at 2-min intervals. (B) Blood gas sampling for monitoring $PaCO_2$, PaO_2 and pH was performed in awake and anesthetized mice.

et al., 2011). We have previously reported on longitudinal measurements using laser-Doppler flowmetry (LDF) and laser-speckle flowmetry (LSF) in awake-behaving mice (Takuwa et al., 2011). Our apparatus could simultaneously measure stable and reproducible CBF responses induced by whisker stimulation and the amount of locomotion over a 1-week period.

In the current study, we investigated the mechanisms underlying CBF regulation in awake mice as compared with anesthetized mice using an LDF system (Takuwa et al., 2011). To the best of our knowledge, no study has investigated the dynamics of red blood cell (RBC) velocity and concentration independently in awake animals, although several studies have reported the hemodynamic response in anesthetized rodents using LDF (Matsuura et al., 1999, 2000, 2001). In the present study, we used the LDF system by which measured RBC velocity and concentration are empirically validated using a thin tube (Kashima et al., 1990, 1993, 1994). We focused on the dynamics of RBC velocity and concentration in cerebral microvessels, key components of CBF, during resting and neuronal activation states under awake and anesthetized conditions.

2. Results

2.1. *Baseline levels of hemodynamics in awake and anesthetized conditions*

Isoflurane anesthesia increased the mean baseline CBF (% increase: 17.7 ± 20.7%), RBC velocity (18.3 ± 16.3%) and concentration levels (2.8 ± 3.3%) as compared with those in awake condition (Fig. 2), but no significant differences between awake and anesthetized conditions were observed. The increase in baseline RBC velocity was relatively larger than that in RBC concentration ($P < 0.05$).

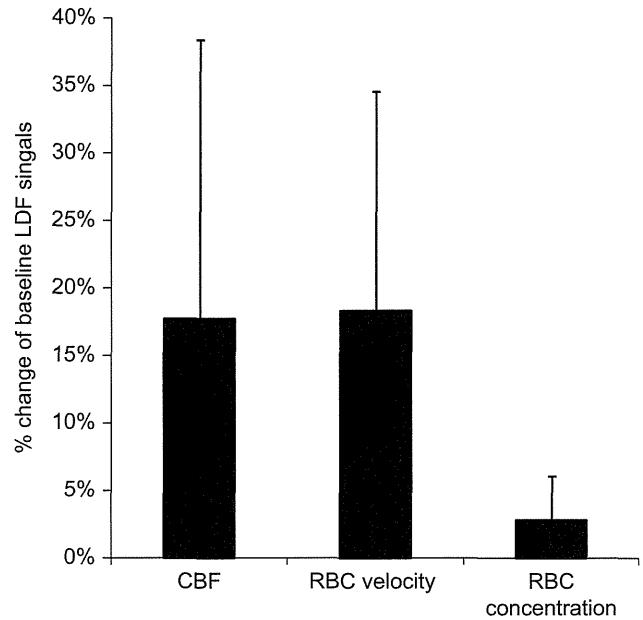

Fig. 2 – Baseline CBF, RBC velocity and RBC concentration under awake and anesthesia conditions ($n = 11$). The baseline values under anesthesia condition were normalized with those under awake condition. Black bars indicate % change in baseline values under isoflurane anesthesia condition. Error bars represent SD.

2.2. *Increases in CBF and RBC velocity and RBC concentration during whisker stimulation*

The response curves of CBF and RBC velocity and concentration in awake condition are shown in Fig. 3. The increases in CBF and RBC velocity and RBC concentration in awake condition were 20.2 ± 6.3%, 18.4 ± 7.5%, and 1.7 ± 2.9%, respectively (Fig. 3A and 4), whereas those in anesthetized condition were 4.8 ± 2.7%, 3.4 ± 2.9%, and 1.4 ± 1.0%, respectively (Figs. 3B and 4). The increases in CBF and RBC velocity in anesthetized condition were significantly lower than those in awake condition ($P < 0.01$), whereas no significant difference was observed in the increase in RBC concentration between anesthetized and awake conditions (Fig. 4).

2.3. *Rise time of response curve in awake conditions*

In each experiment, we calculated the rise time, which indicated the onset time of increase in LDF signals during whisker stimulation (see Section 4). Rise times for the response curves of CBF and RBC velocity and concentration in awake mice were 0.35 s, 0.86 s and 0.35 s, respectively, on average. The rise time of RBC concentration occurred 0.53 s faster than that of velocity. In addition, an acute increase in RBC concentration during stimulation was observed in awake condition (Fig. 3C). The onsets of increase in the response curves of all parameters in anesthetized condition were relatively delayed as compared with those in awake condition (Fig. 3C).

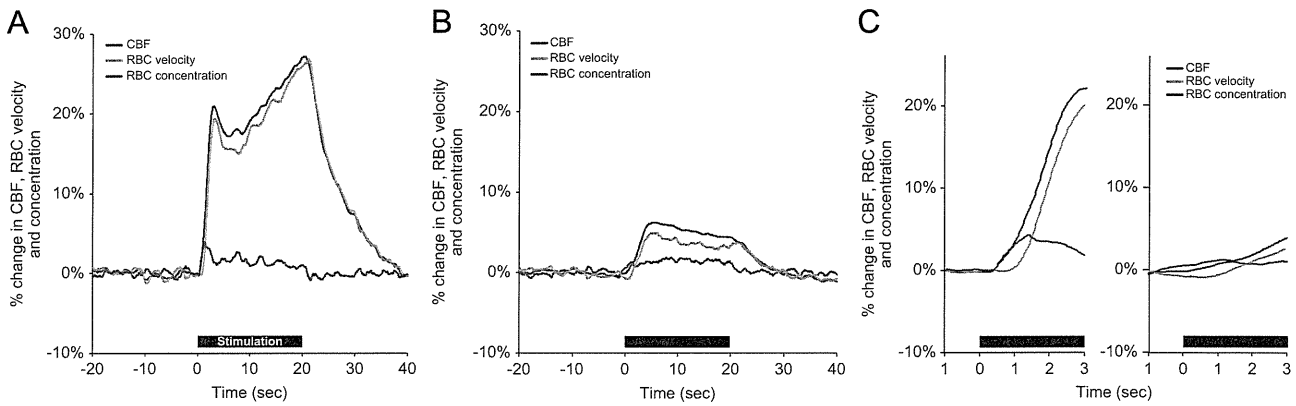

Fig. 3 – Time–response curves for normalized and averaged CBF, RBC velocity and concentration with somatosensory stimulation under awake and anesthesia conditions. Horizontal bars indicate stimulation period. (A) Response curves for CBF, RBC velocity and concentration in awake mice ($n = 12$). These data were normalized to baseline level (20 s before sensory stimulation). Red, green and blue lines indicate % changes in CBF, RBC velocity and concentration, respectively. (B) Response curves for CBF, RBC velocity and concentration in anesthetized mice ($n = 11$). (C) Expanded views of response curves for CBF, RBC velocity and concentration (initial 3-s duration shown). (For interpretation of the references to color in this figure caption, the reader is referred to the web version of this article.)

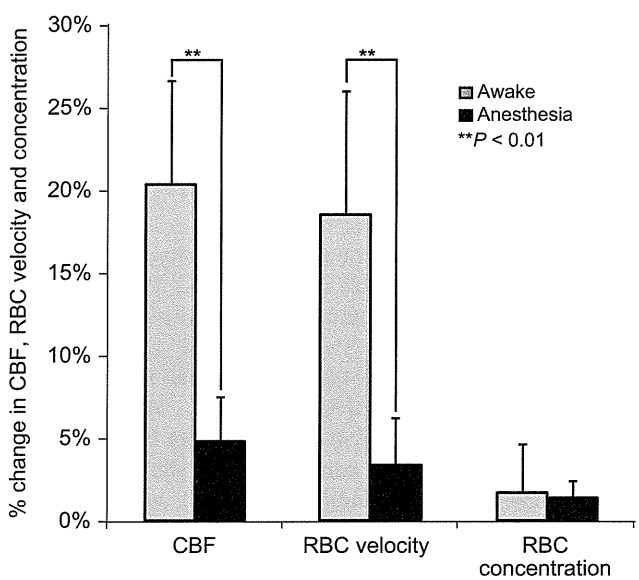

Fig. 4 – The percentage change in CBF, RBC velocity and concentration calculated as averaged values during whisker stimulation (20 s). Gray and black bars indicate increases in CBF, RBC velocity and concentration during whisker stimulation before anesthesia (awake) and after anesthesia (anesthesia), respectively. Error bars indicate SD. $^{**}P < 0.01$.

2.4. *Blood gas values in awake and anesthetized conditions*

$PaCO_2$ and PaO_2 values in anesthetized and awake animals are shown in Table 1. During blood gas sampling, body temperature was maintained at about 37.0 °C. A significant difference in $PaCO_2$ was observed between awake and anesthetized conditions (43.9 ± 6.1 mm Hg and 50.3 ± 5.4 mm Hg, respectively) ($P < 0.05$). There was a significant difference in PaO_2 between awake (129.0 ± 26.8 mm Hg) and anesthetized (182.1 ± 27.5 mm Hg) mice ($P < 0.01$), as isoflurane anesthesia was with O_2 and N_2 mixed gas.

Table 1 – Parameters of blood gas sampling under awake and anesthesia conditions.

Parameters[a] ($n = 6$)	Awake condition[a] ($n = 6$)	Anesthetized condition[a] ($n = 6$)
PaO_2 (mm Hg)	129.0 ± 26.8	182.1 ± 27.5**
$PaCO_2$ (mm Hg)	43.9 ± 6.1	50.3 ± 5.4*
pH	7.38 ± 0.1	7.33 ± 0.1

[a] Number of mice; mean ± SD.
* $P < 0.05$.
** $P < 0.01$.

3. Discussion

Previous studies have verified the validity of RBC velocity and concentration measurements using LDF (Kashima et al., 1990, 1993, 1994). In the present study, a hemodynamic response in the somatosensory cortex to whisker stimulation was observed in both RBC velocity and concentration under awake and anesthesia conditions. Although RBC velocity and concentration were previously measured with anesthetized rodent models in several studies, this is the first observation of the measurement of hemodynamics in awake mice. The increase in CBF during whisker stimulation under awake condition was four times higher than that under anesthetized condition (Figs. 3 and 4) in spite of a relatively stable baseline CBF between the different conditions (Fig. 2). The increase in RBC velocity was far greater than that in RBC concentration under awake condition. Isoflurane-induced anesthesia attenuated both increases in RCB velocity and

concentration during whisker stimulation, and the attenuation of the increase in RBC velocity was relatively large as compared to that of the increase in RBC concentration.

Lee et al. (1994) and Sicard et al. (2003) reported an increase in baseline CBF during isoflurane anesthesia when $PaCO_2$ was controlled within normal range using artificial respiration, suggesting that only isoflurane anesthesia causes vasodilatation in the brain. In addition, hypercapnia was observed in isoflurane anesthetized mice (Table 1). Previous studies reported that hypercapnia causes cerebral vasodilatation and increases the baseline CBF (Kety and Schmidt, 1948; Raper et al., 1971; Shimosegawa et al., 1995). In this study, mean baseline CBF and RBC velocity and concentration under anesthesia condition also increased as compared with those in awake condition, but no statistical difference was observed. The discrepancy between previous reports (Lee et al., 1994; Sicard et al., 2003) and the present study might be due to the effects of hyperoxia on baseline CBF. A significant increase in PaO_2 in anesthetized mouse was observed in this study. It has been reported that acute hyperoxia caused a vasoconstriction of arteriole (Duling and Berne, 1970; Pries et al., 1995) and decreased baseline CBF in a rodent model (Matsuura et al., 2001, 2002). Especially, Matsuura et al. reported a 5.6% decrease in baseline CBF under hyperoxia caused by 100% O_2 inhalation (Matsuura et al., 2001). However, since PaO_2 under anesthesia in our study (182 ± 28 mm Hg) was far lower than that in their report (513.5 ± 48.4 mm Hg), the effects of hypoxia in the current study were considerably lower than those in the previous report. Thus, the increase in baseline CBF was caused by hypercapnia and isoflurane anesthesia, but it might have been attenuated by the effects of hyperoxia.

The increase in RBC velocity during whisker stimulation in awake mice was far greater than that in RBC concentration. Increases in CBF and cerebral blood volume (CBV) during sensory stimulation were previously investigated in humans using PET. Ito et al. (2003) reported an increase in CBF that was greater than that in CBV in the visual cortex by high-frequency visual stimulation in humans, indicating an increase in vascular blood velocity. Of course, RBC concentration was different in observation object from CBV in the PET study, the relationship between RBC velocity and concentration in awake mice might be similar to that between vascular blood velocity and CBV in humans. Thus, a slight change in vessel volume might result in a great effect on RBC velocity.

Antognini et al. (1997) reported that isoflurane anesthesia attenuated the CBF response to sensory stimulation in a human fMRI study. In the present study, we also observed attenuation of the increase in CBF during whisker stimulation under isoflurane anesthesia, indicating that this occurs in both mice and humans. Under isoflurane anesthesia, we observed that attenuation of the increase in RBC velocity was also far greater than the increase in RBC concentration (Figs. 3 and 4). The increase in CBF was caused by a major increase in RBC velocity and a slight change in RBC concentration. The observations also support the above suggestion that a slight vessel volume change will affect RBC velocity.

Anesthesia inhibited the increase in neuronal activation (field potential) with increasing frequency of electrical stimulation in the somatosensory cortex of rats and suppressed the increase in CBF during sensory stimulation (Martin et al., 2006). Based on this finding, we hypothesized that isoflurane anesthesia attenuated the neuronal response to sensory stimulation, resulting in the attenuation of neuronal activation suppressing the increase in CBF due to decrease in energy demand. As a result, the increase in RBC velocity and concentration in anesthetized mice was inhibited. Martin et al. (2006) also reported that anesthesia prolonged the latency to the onset of neuronal response in rats, which is consistent with our finding that the rise time of increase in CBF in anesthesia was later than that in awake condition (Fig. 3).

In conclusion, RBC velocity and concentration were measured in awake and anesthetized mice. The relationship between RBC velocity and concentration in awake mice was similar to that shown in humans using PET. Isoflurane-induced anesthesia attenuated the increase in CBF that was mainly caused by an increase in RBC velocity during stimulation, indicating that decreased energy demand in the brain as a result of the attenuation of neuronal activity with anesthesia might inhibit the increase in RBC velocity and concentration. The RBC measurement techniques in awake animals are likely useful for investigation of the hemodynamic changes caused by changes in neural activity or other chemical factors like $PaCO_2$.

4. Experimental procedures

4.1. *Animal preparation*

All experiments were performed in accordance with the institutional guidelines on humane care and use of laboratory animals and were approved by the Institutional Committee for Animal Experimentation. A total of 18 male C57BL/6J mice (20–30 g, 7–11 weeks; Japan SLC, Inc., Hamamatsu, Japan) were used in two separate experiments: LDF measurements ($n = 12$) and blood gas analysis ($n = 6$). The animals were housed in a 12-h light/dark cycle room at a temperature of 25 °C with ad libitum water and food.

For the surgical procedure, the animals were anesthetized with a mixture of air, oxygen and isoflurane (3–5% for induction and 2% for surgery) via facemask. The animals were fixed in a stereotactic frame, and rectal temperature was maintained at 37.0 °C using a heating pad (ATC-210, Unique Medical Co., Ltd., Tokyo, Japan). A 10-mm midline incision was made to expose the skull over the left somatosensory cortex. The skull (3 mm × 3 mm centered at 1.8 mm caudal and 2.5 mm lateral from bregma) was thinned to translucency using a dental drill. A custom-made metal plate with a 7-mm diameter hole in the center was attached to the skull with dental resin. After completion of the surgery, the animals were allowed to recover from anesthesia and housed for at least one week before initiation of the experiments.

4.2. *Experimental protocols*

The experimental protocol for CBF and locomotion measurements in awake mice was reported previously (Takuwa et al., 2011). Briefly, the metal plate on the animal's head was

screwed to a custom-made stereotactic apparatus. The animal was then placed on a styrofoam ball that was floating using a stream of air. This allowed for the animals to exercise freely on the ball while the animal's head was fixed in the apparatus. CBF was measured from the somatosensory cortex.

LDF measurements were performed under awake and isoflurane-anesthetized conditions. The recording was started under awake condition, followed by anesthetized state (Fig. 1A). To measure the hemodynamic response during anesthetized condition, mice were given 1.5% isoflurane (3% for induction).

4.3. *CBF and RBC velocity and concentration measurements*

CBF was measured with an LDF system (FLO-C1, OMEGAWAVE, Tokyo, Japan) using an LDF probe with a 0.46-mm tip diameter (Probe NS; OMEGAWAVE) placed perpendicular to the barrel cortex in the somatosensory cortex. The probe was attached to the thinned skull of an awake mouse, avoiding areas with large blood vessels (Matsuura and Kanno, 2001). Our LDF system simultaneously provided three parameters: flux (CBF), RBC concentration and RBC velocity, where RBC velocity = CBF/RBC concentration (Nilsson, 1984). The volume of LDF measurement was approximately 1 mm^3 (Nilsson et al., 1980). A sampling rate of 0.1 s was used for measuring all LDF signals (CBF, RBC velocity and concentration).

During CBF measurements, CBF response to neuronal activation was induced by whisker stimulation. An air puff was delivered to all of the right whiskers at a pressure of ~15 psi via a compressed-air bottle. A rectangular pulse stimulation (50-ms pulse width and 100-ms onset-to-onset interval, i.e., 10 Hz frequency) generated with a Master-8 (A.M.P.I., Jerusalem, Israel) was induced for a 20-s duration (Takuwa et al., 2011).

Our previous study using the same procedure as the present experiment revealed that the increase in CBF induced by whisker stimulation in awake mice was quite stable in despite of variable animal locomotion, between daytime and nighttime and over one week (Takuwa et al., 2011). These results indicated that the effect of animal locomotion on the increase in CBF induced by whisker stimulation was negligible. On the other hand, as it is possible that baseline CBF might be affected by excessive exercise during the experiment, we used only the LDF signal data, which were obtained under resting condition.

4.4. *Blood gas analysis*

The tail artery of mice was cannulated for blood gas sampling under isoflurane anesthesia (3% for induction and 2.0% during surgery). Body temperature was monitored with a rectal probe and maintained at approximately 37.0 °C by heating pad (ATC-210; Unique Medical). The mice were fixed in a custom-made stereotactic apparatus and anesthetized with isoflurane via facemask. The protocol used for blood gas sampling is shown in Fig. 1B. Sampling in anesthetized state (1.5% isoflurane) began after approximately 30 min from the completion of surgery to stabilize the experimental conditions (sampling 1 in Fig. 1B). A second sampling was performed 30 min after the cessation of anesthesia, during which the mice had enough time to recover from anesthesia (sampling 2 in Fig. 1B). In the third sampling, mice were anesthetized again, and blood gas sampling was performed 30 min after the induction of anesthesia (sampling 3 in Fig. 1B). These blood samples were analyzed by blood analyzer (I-STAT; Abbott, IL, USA) under awake and anesthetized conditions. $PaCO_2$, PaO_2 and pH were measured at every sampling. To remove the effect of surgery on the blood gas condition, the values in samplings 1 and 3 were averaged. These averaged values, obtained from anesthetized mice, were statistically compared with those of awake mice (T-test).

4.5. *Data analysis*

During the experiments, LDF data were recorded using a polygraph data acquisition system (MP150; BIOPAC Systems, Inc., Goleta, CA, USA) and analyzed offline. For the time-course data of CBF and RBC velocity and concentration, the LDF signal was normalized toward a baseline level of each signal. Twenty-second pre-stimulus values of each signal were defined as baseline CBF and RBC velocity and concentration. The time-course data in each trial were then averaged across all trials in each animal. In this study, the rise times of increase in CBF and RBC velocity and concentration during whisker stimulation were determined as the first time greater than mean plus three times of the standard deviation of the averaged baseline, which was obtained within 20 s before whisker stimulation. We compared the rise time in the response curve between different parameters in awake mice.

For calculation of the percentage change of increases in CBF, RBC velocity and concentration, each LDF parameter (CBF, RBC velocity and concentration), which were normalized to the respective baseline values, was averaged within the whisker stimulation period (percentage change of LDF parameters = LDF parameters (activation)/LDF parameters (baseline) – 1). The increases in CBF, RBC velocity and concentration during whisker stimulation were obtained from awake and anesthetized conditions. These conditions were statistically analyzed by paired t-test.

Role of the funding source

There are no roles of the sponsors in the performance of the research or preparation of the paper.

Contributors

H.T., T.M., and H.I. designed research; H.T., and T.M. performed research; H.T., T.M., I.K., and H.I. analyzed data; I.K., and T.O. helped data interpretation and discussion; and H.T., T.M., and H.I. wrote the paper.

Acknowledgments

The assistance of members of the National Institute of Radiological Sciences in performing the LDF experiments is gratefully acknowledged.

REFERENCES

Antognini, J.F., Buonocore, M.H., Disbrow, E.A., Carstens, E., 1997. Isoflurane anesthesia blunts cerebral responses to noxious and innocuous stimuli: a fMRI study. Life Sci. 61, 349–354.

Duling, B.R., Berne, R.M., 1970. Longitudinal gradients in periarteriolar oxygen tension. Circ. Res. 27, 669–678.

Ito, H., Kanno, I., Ibaraki, M., Hatazawa, J., Miura, S., 2003. Changes in human cerebral blood flow and cerebral blood volume during hypercapnia and hypocapnia measured by positron emission tomography. J. Cereb. Blood Flow Metab. 23, 665–670.

Kashima, S., Nishihara, M., Takemoto, Y., Ohsawa, T., 1990. Relationship between the integrated intensity of the power spectrum of scattered light and tissue blood volume by the dynamic light scattering method. Jpn. J. Appl. Phys. 29, 1862–1865.

Kashima, S., Sohda, A., Takeuchi, H., Ohsawa, T., 1993. Study of measuring the velocity of erythrocytes in tissue by the dynamic light scattering method. Jpn. J. Appl. Phys. 32, 2177–2182.

Kashima, S., Oka, S., Ishikawa, J., Ohsawa, T., Hiki, Y., 1994. Measurement of tissue blood volume in a model system and in the canine intesitne by dynamic light scattering. Lasers Life Sci. 6, 79–91.

Kety, S.S., Schmidt, C.F., 1948. The effects of altered arterial tensions of carbon dioxide and oxygen on cerebral blood flow and cerebral oxygen consumption of normal young men. J. Clin. Invest. 27, 484–492.

Lahti, K.M., Ferris, C.F., Li, F., Sotak, C.H., King, J.A., 1999. Comparison of evoked cortical activity in conscious and propofol-anesthetized rats using functional MRI. Magn. Reson. Med. 41, 412–416.

Lee, J.G., Hudetz, A.G., Smith, J.J., Hillard, C.J., Bosnjak, Z.J., Kampine, J.P., 1994. The effects of halothane and isoflurane on cerebrocortical microcirculation and autoregulation as assessed by laser-Doppler flowmetry. Anesth. Analg. 79, 58–65.

Martin, C., Berwick, J., Johnston, D., Zheng, Y., Martindale, J., Port, M., Redgrave, P., Mayhew, J., 2002. Optical imaging spectroscopy in the unanaesthetised rat. J. Neurosci. Methods 120, 25–34.

Martin, C., Martindale, J., Berwick, J., Mayhew, J., 2006. Investigating neural-hemodynamic coupling and the hemodynamic response function in the awake rat. Neuroimage 32, 33–48.

Matsuura, T., Fujita, H., Seki, C., Kashikura, K., Yamada, K., Kanno, I., 1999. CBF change evoked by somatosensory activation measured by laser-Doppler flowmetry: independent evaluation of RBC velocity and RBC concentration. Jpn. J. Physiol. 49, 289–296.

Matsuura, T., Fujita, H., Kashikura, K., Kanno, I., 2000. Evoked local cerebral blood flow induced by somatosensory stimulation is proportional to the baseline flow. Neurosci. Res. 38, 341–348.

Matsuura, T., Kanno, I., 2001. Changes in red blood cell behavior during cerebral blood flow increase in the rat somatosensory cortex: a study of laser-Doppler flowmetry. Jpn. J. Physiol. 51, 703–708.

Matsuura, T., Kanno, I., 2002. Effect of nitric oxide synthase inhibitor on the local cerebral blood flow evoked by rat somatosensory stimulation under hyperoxia. Comp Biochem Physiol A Mol Integr Physiol 131, 267–274.

Matsuura, T., Kashikura, K., Kanno, I., 2001. Hemodynamics of local cerebral blood flow induced by somatosensory stimulation under normoxia and hyperoxia in rats. Comp. Biochem. Physiol. A: Mol. Integr. Physiol. 129, 363–372.

Mizuma, H., Shukuri, M., Hayashi, T., Watanabe, Y., Onoe, H., 2010. Establishment of in vivo brain imaging method in conscious mice. J. Nucl. Med. 51, 1068–1075.

Nilsson, G.E., 1984. Signal processor for laser Doppler tissue flowmeters. Med. Biol. Eng. Comput. 22, 343–348.

Nilsson, G.E., Tenland, T., Öberg, P.A., 1980. Evaluation of a laser Doppler flowmeter for measurement of tissue blood flow. IEEE Trans. Biomed. Eng. 27, 597–604.

Peeters, R.R., Tindemans, I., De Schutter, E., Van der Linden, A., 2001. Comparing BOLD fMRI signal changes in the awake and anesthetized rat during electrical forepaw stimulation. Magn. Reson. Imaging 19, 821–826.

Pries, A.R., Heide, J., Ley, K., Klotz, K.L., Gaehtgens, P., 1995. Effect of oxygen tension on regulation of arteriolar diameter in skeletal muscle in situ. Microvasc. Res. 49, 289–299.

Raper, A.J., Kontos, H.A., Patterson Jr., J.L., 1971. Response of pial precapillary vessels to changes in arterial carbon dioxide tension. Circ. Res. 28, 518–523.

Schulz, D., Southekal, S., Junnarkar, S.S., Pratte, J.F., Purschke, M.L., Stoll, S.P., Ravindranath, B., Maramraju, S.H., Krishnamoorthy, S., Henn, F.A., O'Connor, P., Woody, C.L., Schlyer, D.J., Vaska, P., 2011. Simultaneous assessment of rodent behavior and neurochemistry using a miniature positron emission tomograph. Nat. Methods 8, 347–352.

Shimosegawa, E., Kanno, I., Hatazawa, J., Fujita, H., Iida, H., Miura, S., Murakami, M., Inugami, A., Ogawa, T., Itoh, H., 1995. Photic stimulation study of changing the arterial partial pressure level of carbon dioxide. J. Cereb. Blood Flow Metab. 15, 111–114.

Sicard, K., Shen, Q., Brevard, M.E., Sullivan, R., Ferris, C.F, King, J.A., Duong, T.Q., 2003. Regional cerebral blood flow and BOLD responses in conscious and anesthetized rats under basal and hypercapnic conditions: implications for functional MRI studies. J. Cereb. Blood Flow Metab. 23, 472–481.

Takuwa, H., Masamoto, K., Obata, T., Kanno, I., 2010. Neurovascular coupling studies in awake-behaving mice. Hirosaki Med. J. 60, 192–196.

Takuwa, H., Autio, J., Nakayama, H., Matsuura, T., Obata, T., Okada, E., Masamoto, K., Kanno, I., 2011. Reproducibility and variance of a stimulation-induced hemodynamic response in barrel cortex of awake behaving mice. Brain Res. 1369, 103–111.

Microvascular Research 84 (2012) 178–187

Contents lists available at SciVerse ScienceDirect

Microvascular Research

journal homepage: www.elsevier.com/locate/ymvre

Image-based vessel-by-vessel analysis for red blood cell and plasma dynamics with automatic segmentation

Hiroshi Kawaguchi [a], Kazuto Masamoto [a,b,*], Hiroshi Ito [a], Iwao Kanno [a]

[a] Molecular Imaging Center, National Institute of Radiological Sciences, 4-9-1 Anagawa, Inage, Chiba 263-8555, Japan
[b] Center for Frontier Science and Engineering, University of Electro-Communications, 1-5-1 Chofugaoka, Chofu, Tokyo 182-8585, Japan

ARTICLE INFO

Article history:
Accepted 1 May 2012
Available online 12 May 2012

ABSTRACT

The aim of the present study was to test the hypothesis that vascular tones of cortical surface and parenchymal blood flow can be dissociated depending on the perturbation. To this end, a novel image-based analytical method for quantitatively measuring vessel diameters and flow dynamics was developed. The algorithm relies on the spatiotemporal coherence of the pixel intensity changes induced by the transit of the fluorescent signals measured using confocal laser scanning fluorescent microscopy in the rat cerebral cortex. A cocktail of fluorescently labeled red blood cell (RBC) and plasma agents was administered to simultaneously compare RBC and plasma dynamics in the same vascular networks. The time to fluorescent signal appearance and the width of the fluorescent signal were measured in each segment and compared between sodium nitroprusside-induced global and sensory stimulation-induced local perturbation conditions. We observed that infusion of sodium nitroprusside induced significant vasodilation in the surface artery, particularly in the small arteries (1.8-fold increase). Vasodilation induced by sensory stimulation was observed to depend on vessel size, but significant changes were only detected for the small arteries and veins. Measurements of the time to venous appearance revealed that appearance time was extended by sodium nitroprusside, but shortened during forepaw stimulation, relative to the control condition. Both perturbations provoked the largest changes between the small artery and vein segments, indicating that the changes in the appearance time originate from blood passage through parenchymal microcirculation. These findings support the hypothesis that cortical surface vascular tone and parenchymal blood flow are individually coordinated.

Introduction

It is well known that the network structure of the cerebral vasculature differs between the cortical surface and parenchymal tissue (Mchedlishvili, 1986). On the surface, arteries have mesh-like anastomosis (i.e., arterio-arterial anastomosis), but no capillaries are present (Schaffer et al., 2006). In the parenchyma, each arteriole forms a terminal arteriole that governs a unit of microvascular networks (Nishimura et al., 2007), and capillary density roughly matches metabolic activity of glucose in the region (Borowsky and Collins, 1989). These morphological features have been thought to play a critical role in coordinating the spatial balance of blood flow supply to meet the localization of the brain functions (i.e., region-specific demand).

It has been proposed that the cortical surface arteries have a major role in controlling the parenchymal blood flow (Mchedlishvili, 1986; Rosenblum and Kontos, 1974). This view was supported by the findings of the parallel changes in parenchymal blood flow and vascular tone of cortical surface arteries during both systemic perturbations induced with an inhalation of 5% carbon dioxide in air and systemic hypertension (Haberl et al., 1989a). However, a dissociation of the surface artery and parenchymal blood flow responses were also found for perturbation induced with topically applied vasoactive agents (Haberl et al., 1989b). These findings indicate that different blood flow regulation mechanisms may exist depending on global and local perturbation.

To test the hypothesis that vascular tone of cortical surface and parenchymal blood flow can be dissociated depending on the perturbation, the present study developed a novel image-based analytical method with high-speed laser scanning confocal microscopy. The algorithm relies on the spatiotemporal coherence of the pixel intensity changes induced by a transit of the fluorescent agents through the time-lapse images captured on the cortical surface of the rats (Autio et al., 2011). To further determine the detailed microcirculation properties, a cocktail of fluorescently labeled red blood cell (RBC) and quantum dot (Qdot) as a plasma marker was administered. The individual vessel widths and transit times of the both RBC and plasma signals were then determined to characterize their vessel-by-vessel

* Corresponding author at: Center for Frontier Science and Engineering, University of Electro-Communications, 1-5-1 Chofugaoka, Chofu, Tokyo 182-8585, Japan. Fax: +81 42 443 5930.
E-mail address: masamoto@mce.uec.ac.jp (K. Masamoto).

0026-2862/$ – see front matter © 2012 Elsevier Inc. All rights reserved.
doi:10.1016/j.mvr.2012.05.001

responses to either systemic global or local perturbations induced with intravenous administration of sodium nitroprusside (SNP) or with electrical forepaw stimulation, respectively.

Materials and methods

Animal preparation

The protocols of all animal experiments were approved by the Institutional Animal Care and Use Committee, and all experiments were carried out in accordance with the institutional guidelines for conducting of animal experiments. A total of five male Sprague–Dawley rats (7–9 weeks, 270–340 g) were used for the experiments. Each animal was initially anesthetized with isoflurane (4–5% for induction and 1.8–2.2% for surgery), and intubation was performed for mechanical ventilation. Three catheters were inserted in the femoral artery, femoral vein, and external carotid artery for systemic arterial blood pressure monitoring and blood sampling, drug infusion, and administration of fluorescent agents, respectively. Each anesthetized animal was secured with a stereotactic apparatus (SG-3N, Narishige, Tokyo, Japan), and the skull over the somatosensory area (3 mm by 3 mm) was removed (Park et al., 2008). The dura was also thinned to enhance translucency, but a thin layer was preserved to maintain cortical microcirculation homeostasis. The exposed cortex was then covered with warmed saline.

After all surgery was completed, the isoflurane concentration was reduced to 1.3–1.5% (Masamoto et al., 2007), and the animal's condition was stabilized for 1 h prior to the measurements. The respiration rate was fixed at 0.87 Hz, and the ventilatory volume was adjusted to maintain end-tidal CO_2 levels (35–42 mm Hg) and blood gas conditions ($PaO_2 = 128 \pm 25$ mm Hg, $PaCO_2 = 35 \pm 3$ mm Hg, pH = 7.40 ± 0.09, Hct = 42 ± 2%). The end-tidal gas and arterial blood gas conditions were measured with a capnograph monitor (V9400, Smiths Medical PM, Inc., Norwell, MA) and a blood gas analyzer (i-STAT 300F Analyzer, i-STAT Corporation, East Windsor, NJ), respectively. Body temperature, measured rectally, was maintained at 37 °C with a heating pad (TR-200, Fine Science Tools Inc., Foster City, CA).

Time-lapse imaging

A cocktail of Qdot 605 (1 μM in stock solution with saline, Invitrogen, San Diego, CA) and fluorescently-labeled RBCs that were collected from a donor rat and incubated with fluorescein isothiocyanate (FITC) (Seylaz et al., 1999), was injected using syringe pump (PHD4400, Harvard Apparatus, MA) into the external carotid artery at a rate of 2.2 mL/min with an injection volume of 0.02 mL (i.e., about 0.5-s duration for one-shot injection) in which hematocrit level was preliminarily adjusted to be within physiologic limits. A previous study has shown this type of water-soluble Qdot (negatively charged) can be used as an analogous agent to the conventionally used fluorescent dextrans (Larson et al., 2003). Thus, we assumed that Qdot represents plasma flow. Images were captured at the cortical surface with a laser scanning confocal microscope (TCS SP5, Leica Microsystems Gmbh, Wetzlar, Germany) with a 5× objective lens (PL FLUOTAR 0.12 NA, Leica Microsystems Gmbh, Wetzlar, Germany). The excitation light was 488 nm Argon, while the emission signal was detected with two photomultiplier tubes (R6357, Hamamatsu Photonics KK., Hamamatsu, Japan) for simultaneous detection of FITC-RBC and Qdot-plasma through an emission filter of 545/90 nm and 605/20 nm, respectively. For Qdot detection channel, a narrow spectrum emission filter was set and the gain level of the detector was adjusted to minimize potential contamination of the signals from FITC which has a relatively broad emission spectrum (480 to 620 nm at 5% of the peak). The size of each single plane image was 512 by 512 pixels (field of view: 1.82 mm by 1.82 mm), and fast time-lapse imaging was performed at a frame rate of 14.2 fps (i.e., 70.4-ms interval for onset to onset) with a total acquisition time of 18 s (256 frames). Due to the low numerical aperture of the lens, the resolution in the depth direction was approximately 50 μm and the lateral resolution was approximately 3 μm under our experimental conditions.

Global and local perturbation

Global perturbation was induced with an intravenous injection of sodium nitroprusside (SNP; 2.2 mg/kg body weight), a well-known vasodilator (Auer, 1978). After blood pressure was stabilized (40 to 50 mm Hg) following the SNP injection, time-lapse imaging was initiated. Previous studies have confirmed that under these ranges of systemic blood pressure, evoked neural activity and oxygen metabolic rate are preserved, and only the evoked vascular response is suppressed (Fukuda et al., 2006; Masamoto et al., 2008).

Local perturbation was given by electrical pulse stimuli (1.0 ms width and 1.5–1.7 mA current with 6 Hz frequency for 25 s) to the forepaw via two needles implanted under the skin in the contra-lateral side of the measurement (Kim et al., 2010; Masamoto et al., 2007). The active area was preliminarily identified by measuring the area of arterial dilation responding to forepaw stimulation. The measurements were started 5 s after the onset of forepaw stimuli, when the evoked hemodynamic changes were observed to reach a plateau.

In each perturbation experiment, between one and four measurements were repeatedly conducted, and a total of four to nine measurements were performed in each animal. In these experiments, mean arterial blood pressure was 97 ± 11 and 45 ± 1 mm Hg under control and SNP conditions, respectively (N = 3 animals), and 93 ± 3 and 94 ± 3 mm Hg under control and forepaw stimulation conditions, respectively (N = 3 animals).

Measurement of appearance and disappearance times

Image analysis was performed with custom-written software (MATLAB, The Mathworks, Natick, MA) after all images were transferred to a computer workstation. First, the times of appearance and disappearance of the fluorescent agent were determined on a per-pixel basis. Since the original raw images involved shot noises from the photomultiplier tube, temporal smoothing was performed every 5 frames on each pixel's raw data. The mean and standard deviation of the baseline intensity were calculated for several tens of frames obtained from the beginning of the measurement. The appearance time was determined as the earliest time point where the pixel intensity surpassed the mean + 3SD of the baseline intensity. Similarly, the disappearance time, the latest time point where the intensity decreased to baseline, was determined by applying the same pixel intensity criterion to the data with time reversed (so that the end became the beginning). For the original (non-reversed) data, the temporal origin (t = 0) was set at the earliest time point in the image for the appearance of the plasma agent measured under control conditions.

Automatic segmentation

In imaging analysis, a minimum unit can be a single pixel; however, pixel-to-pixel comparison is not valid for images containing displacement of the signal location, such as during vasodilation or vasoconstriction. This study instead used a single vessel segment as a minimum unit, which overcomes this limitation for comparing images obtained at different conditions. First, an extraction of the vessel area was made by determining appearance time measured for all 512 by 512 pixels in the image. If the appearance time was assigned as null, the pixel was regarded as being in the non-vessel area (i.e., tissue area). Second, the vessel area was divided into

either artery or vein clusters, based on the differences of their appearance time. A histogram of the appearance time typically showed a bimodal distribution (i.e., originating from artery and vein differences). However, this does not necessarily mean that the pixels showing the earlier appearance time were all belong to artery components and vice versa (e.g., for the smallest artery and vein components). Thus, the present study focused on the spatiotemporal continuity of the signal appearance within and among the connecting vessels to achieve a complete separation of the artery and vein segments. To this end, an iterative region-growing procedure was applied to cluster similar appearance time areas into the respective large artery and vein areas which showed two predominant components in the histogram of appearance time. The vessel area was first subdivided into 8 components whose appearance time was identical. Then, the components were organized in ascending order according to their size (i.e., number of pixels), and the component that had the smallest size was merged into the adjacent component that had the closest appearance time. If there were several candidates that had equally close appearance time, the largest component among the candidates was selected. Then, the appearance time in the smallest component was replaced to that of the merged component, and the histogram of appearance time was updated. These iterations were repeated until two separate clusters (i.e., artery and vein compartments) appeared in the histogram. Finally, the cluster that had the earlier appearance time was assigned as an artery area, and another cluster was assigned as a vein area. Based on these clustering methods, the vessel area was segmented and the separation of artery and vein segments was visually confirmed by comparing the segmented image with the original raw image.

If necessary, the manual correction was made for artery and vein segmentation. For example, an intersection of the artery and vein caused discontinuous vessel segmentation. In the case of a vein apparently crossing over an artery, the edges of venous segments along the intersection were invaded by arterial signals that passed under the venous trunk because of low absorption effects near the side of the vein. To correct this error, the two discontinuous portions of the arterial segment were manually connected to recover the artery segments lost under the vein segment. If the artery crossed over a vein, the discontinuous vein segment was present in the appearance time image. Because the crossing area was a mixture of the artery and vein appearance time signals, the lost portions of the venous segments were recovered based on the disappearance time image. Alternatively, the mixed signals of the arterial and venous components in these crossing areas can be deconvoluted into the original arterial and venous signals, if a whole time-course of the fluorescent signals was available and the both signals from connecting arteries and veins to the crossing areas were detectable. However, due to a lack of the whole time-course data, only manual correction for segmentation was made possible, but no further analysis for these crossing areas was made in the present study.

The last step of the segmentation procedure was to define a single vessel segment which had two branches at both ends. First, artery and vein images were thinned in the longitudinal direction of the vessel tree. Then, the thinned vessels were segmented with a part-type segmentation method for articulated voxel shapes (Reniers et al., 2008) with modifications for two-dimensional images. To determine the branching pattern of the vessel, a geodesicness measure (γ) was computed at each pixel on the vessel segments except for the junctions and endpoints (Reniers et al., 2008). For example, if the target segment vessels had a high geodesicness measure (e.g., γ = nearly 1), those vessels were judged as running in parallel to the vessel wall and thus defined as a single segment. If their geodesicness was low (e.g., $\gamma = 0.5$–0.8), the vessels were considered as two separate vessels (i.e., two segments) (see also Supplemental Fig. S1 which represent the results of segmentation from the raw image shown in Fig. 1a). These segmentation tools we made are disclosed in Matlab Central (http://www.mathworks.com/matlabcentral/fileexchange/36031-vessel-branch-segmentation).

Measurement of passage width

The width of the vessel segment, i.e., the spatial width of the contrast agent's passage, was measured in each vessel segment. First, a Euclidean distance technique was applied for all segmented vessels to measure the gross distance from the edge of the vessel segment to the thinned vessels along the longitudinal direction of the vessel segment. Then, the mean of the largest 5% of distances (i.e., the farthest points from the edge of the vessel wall) was measured and doubled to compute the width. Also, the area of the segmentalized vessels was measured and represented by the number of pixels. Finally, each vessel segment was indexed with an identical number across different imaging sessions, i.e., control, global (SNP), and local (forepaw) perturbation in each animal, by referring to a plasma flow image obtained under control conditions. Then, all vessel segments were sorted into 6 categories by referencing the width of the plasma passage (i.e., the lumen diameter): small (SA; <25 μm), medium (MA; >25, <50 μm), and large arteries (LA; >50 μm), and small (SV, <50 μm), medium (MV, >50, <100 μm) and large veins (LV, >100 μm).

Statistics

Statistical analysis was performed using custom MATLAB scripts. A Student's *t*-test was applied to evaluate the changes in diameter and appearance time between control and perturbation conditions for each vascular segment. Bonferroni corrections were performed for comparisons among 6 vascular segments. A p-value of less than 0.05/6 was considered statistically significant. Data were represented as mean ± standard deviation.

Results

Imaging the spatiotemporal evolution of fluorescent agents

Time-lapse images of the fluorescent agents showed distinct differences between the fluorescent signal changes in artery and vein compartments (Fig. 1a). The apparently similar spatiotemporal behaviors were seen for the RBC and plasma markers (Fig. 1a). The changes in signal intensity were sufficient to determine both appearance and disappearance times on a single-pixel basis after removal of shot noises (Fig. 1b). However, due to a limited dynamic range, the peak intensity was not measurable in our experimental condition (i.e., a lack of a whole time–intensity curve). The reconstructed images for both appearance and disappearance times showed detailed spatiotemporal evolution of the injected fluorescent agents within and across the vascular networks (Figs. 1c and d).

In arterial compartments, relatively uniform appearance and disappearance times were seen for all vessel sizes. In contrast, the veins showed different patterns depending on the size of the vessels. Small veins had a relatively homogeneous pattern and fast appearance and disappearance times, whereas medium and large veins showed a stripe pattern of passage times that continued from their individual daughter veins along the vessel wall. In these vessels, the stripe patterns were observed to be unmixed in a radial direction within the vessel segment, indicating a parallel flow.

Automatic segmentation and representative histogram

The spatiotemporal continuity of the fluorescent signal dynamics was used for automated segmentation of the artery and vein

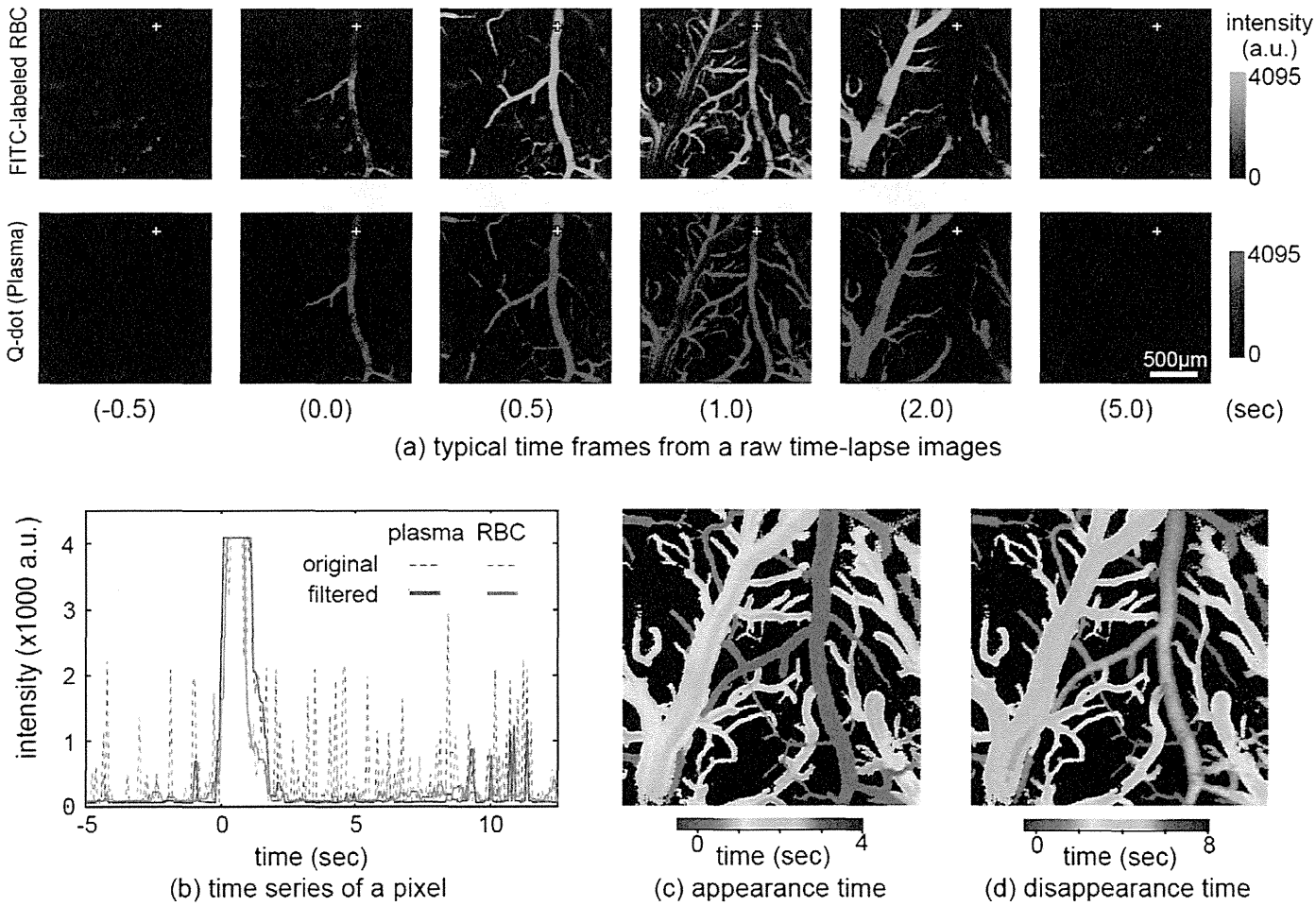

Fig. 1. Imaging and measurement of spatiotemporal fluorescent signal changes. (a) Representative time-lapse images for the transit of FITC-labeled RBC (green, upper) and Qdot plasma markers (red, bottom) measured using confocal laser scanning microscopy in the rat cerebral cortex. The fluorescent agents first appeared in the artery (time 0) and then propagated to the small to large veins. No detectable differences were seen between the RBC and plasma dynamics. (b) Time series of pixel intensity changes measured at a single pixel ("+") shown in (a). The raw signal intensity is shown as dotted lines for the RBC (green) and plasma (red) images. Signal intensity changes were sufficient to determine both appearance and disappearance times after filtering the shot noises (straight line). Representative images for the appearance (c) and disappearance (d) times measured on a single-pixel basis shown in (a). Fast appearance and disappearance were observed in the arterial vessels (red), whereas the large veins (green to blue) had slow appearance and disappearance. Note that longitudinal traces along the vessel were seen for the large veins, indicating the parallel flow in these vessels.

compartments (Fig. 2a). From all five animals, we obtained a total of 423 vessel segments (i.e., 145 artery and 278 vein segments, Table 1), which can be considered as a sufficient number of samples for comparative statistical analysis between control and perturbation conditions. The mean pixel occupancy per image was 7.1%, 4.1%, and 0.7% for the arterial segments LA, MA, and SA, respectively, whereas it was 5.0%, 8.8%, and 21% for the venous segments SV, MV, and LV, respectively (Table 1). The mean number of the vessels analyzed for all 6 segments is also summarized in Table 1. In case of mis-prediction after automated segmentation, such as for an intersection of an artery and a vein, manual corrections were made with reference to the original time-lapse images (Fig. 2b).

The appearance time histogram showed two sharp peaks corresponding to the artery and vein signals (Fig. 2c). In contrast, the disappearance time histogram showed a broad, mixed distribution (Fig. 2d). Because the mixture of the artery and vein signals makes it difficult to differentiate the two, only appearance time results were used for later analysis.

Global perturbation

Comparison between control (Fig. 3a1) and SNP conditions (Fig. 3a2) showed an increase in the fluorescent agent passages after SNP induction, largely in the arterial side. The average increases in the arterial widths were 9 ± 7 and 5 ± 7 μm for the RBC and plasma passages, respectively, in this representative animal, where the arterial baseline widths were 24 ± 13 and 31 ± 13 μm for the RBC and plasma passages, respectively (Fig. 3b1). On the other hand, the venous vessel RBC and plasma widths were 54 ± 59 and 60 ± 60 μm, respectively, under control conditions, and 56 ± 60 and 58 ± 59 μm, respectively, under SNP conditions (Fig. 3b2). The statistically significant ($p<0.01/4$, paired *t*-test with Bonferroni correction) increase in the width changes due to SNP were detected for the arterial compartment, but not the venous side, in both RBC and plasma measurements. It should be noted that a relatively wide width was detected for the plasma compared to the RBC passages (Figs. S2a1 and S2a2).

A marked increase in the appearance time was also detected in all vein segments after SNP injection (Figs. 3a1 and a2). The average increase was 1.4 ± 0.5 and 1.5 ± 0.6 s for RBC and plasma, respectively, in the veins (Fig. 3c2), whereas it was 0.25 ± 0.22 and 0.28 ± 0.19 s in the arteries (Fig. 3c1). Tease differences between the control and SNP conditions were statistically significant ($p<0.01/4$) for both artery and vein components. Consequently, the difference in the mean appearance time between artery and vein compartments also increased: control vs. SNP appearance times were 1.0 vs. 2.2 s for

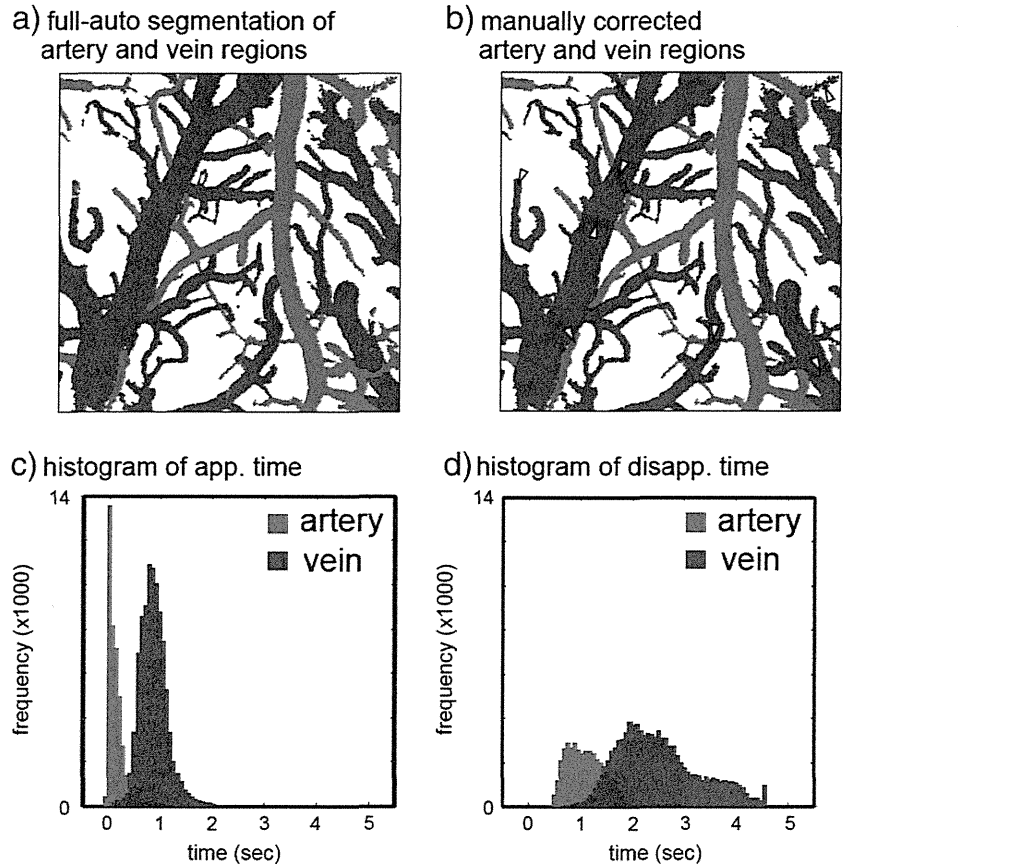

Fig. 2. Segmentation and histogram measurements. (a) Representative raw images after automatic segmentation. The artery (red) and vein (blue) areas were masked out by the region-growing technique by referencing appearance time results. (b) The masks were manually corrected for intersection and error regions (arrowheads) by referencing the original time-lapse image. Histograms of the appearance and disappearance times are shown in (c) and (d), respectively. The red and blue populations represent the pixels in the arterial and venous masked regions, respectively. Due to the large overlap of the artery and vein pixels in the disappearance time measurements, only the appearance time measurements were used for later analysis.

RBC and 0.8 vs. 2.1 s for plasma, indicating an extended traveling time through parenchymal microcirculation under SNP conditions. The similar trend was detected in the changes of appearance time for RBC and plasma in the both arteries (Supplemental Fig. S2b1) and veins (Supplemental Fig. S2b2).

Local perturbation

Width changes of the fluorescent signal passages were not evidently observed for the response to forepaw stimulation (Fig. 4a2) relative to the control condition (Fig. 4a1). Vessel-by-vessel comparisons showed that the widths under control vs. local perturbation conditions were 40 ± 17 vs. 37 ± 18 μm for RBC and 42 ± 17 vs. 42 ± 18 μm for plasma in arteries (Fig. 4b1), and 57 ± 60 vs. 59 ± 60 μm for RBC and 64 ± 59 and 63 ± 58 μm for plasma in veins (Fig. 4b2), respectively. On the other hand, the venous appearance time decreased (0.7 ± 0.2 s) equally for both RBC and plasma (Fig. 4c2), whereas the mean difference in the arterial appearance time between control and forepaw stimulation was 0.17 ± 0.09 s and 0.13 ± 0.07 s for RBC and plasma (Fig. 4c1), respectively. The similar trend was detected in the width changes (Supplemental Figs. S3a1 and a2) and appearance time (Supplemental Figs. S3b1 and b2) between RBC and plasma passages.

Width changes: global vs. local perturbation

Population data showed that global perturbation induced significant vasodilation in the arteries (15 ± 9 and 15 ± 12 μm) as well as the veins (10 ± 8 and 7 ± 10 μm) for both RBC and plasma, respectively. These changes were uniform among the vessel segments, leading to relatively higher change ratios in the small arteries due to the smaller widths at their baseline (Fig. 5a1). The SA compartment showed average increases of 89% and 79% in the RBC and plasma

Table 1
Segmented vessel properties (N = 5).

	LA	MA	SA	SV	MV	LV
Mean width (μm)	64 ± 6	35 ± 2	19 ± 3	32 ± 3	66 ± 1	188 ± 35
Total number of vessels	23	73	49	176	75	27
Mean number of vessels per image	5 ± 2	15 ± 8	10 ± 5	35 ± 9	15 ± 4	5 ± 2
Mean number of pixels per vessel	4540 ± 1957	713 ± 160	212 ± 75	359 ± 73	1644 ± 556	$10{,}339 \pm 3417$
Mean occupancy per image (%)	7.1 ± 2.6	4.1 ± 3.0	0.7 ± 0.3	5.0 ± 2.1	8.8 ± 1.4	21 ± 8

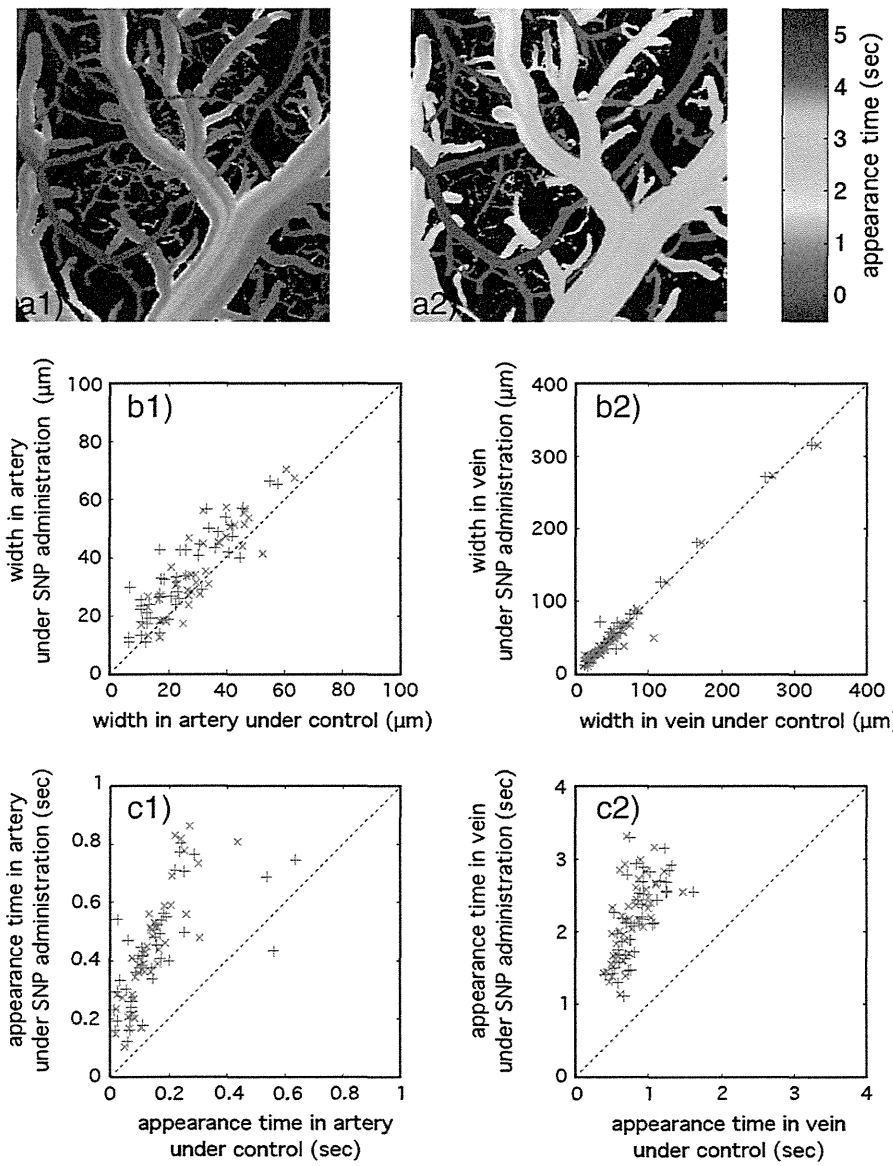

Fig. 3. Representative results for global perturbation measurements (N = 1). (a) Plasma appearance times are shown for control (a1) and SNP (a2) conditions. The color differences between the two images indicate the SNP-induced increase in the venous appearance time (orange/yellow to green/blue). Further, the SNP induced vasodilation in both the arterial (red) and venous segments (orange/green). (b) A comparison of the width changes induced by SNP for all arterial (b1) and venous (b2) segments. A consistent increase in the width was seen for both the RBC (green "+") and plasma (red "x") passages. (c) A comparison of the appearance time measurements. The SNP increased the appearance time slightly in the arteries (c1) and increased the appearance time greatly in the veins (c2).

widths, respectively: these were the largest changes among all 6 vessel segments. For local perturbation (Fig. 5b1), large arteries and veins showed no significant changes in width for either RBC (1.7 ± 4.7 and -0.2 ± 5.8 μm) or plasma (1.9 ± 5.1 and 0.5 ± 5.6 μm), while the small arteries and veins showed significant dilation (2.3 ± 4.9 and 2.3 ± 4.2 μm for RBC and 4.1 ± 4.1 and 2.7 ± 6.0 μm for plasma, respectively). As a result, the SA had the highest increases in the vessel width induced by local perturbation; 13% and 18% increase for RBC and plasma, respectively.

Appearance time changes: global vs. local perturbation

Dependence on vessel size was not observed for changes in appearance time induced by either global (SNP injection) or local (forepaw stimulation) perturbations. SNP injection induced a relatively uniform increase in the venous appearance time (Fig. 5a2). A significant increase was observed in the MA, SA, SV, and MV compartments (0.2 to 1.0 s). In contrast, forepaw stimulation significantly shortened the venous appearance time (−0.5 to −0.4 s, Fig. 5b2). The SA and SV compartments consistently had the largest gap for both perturbations, indicating that the changes in the appearance time mostly originate from parenchymal microcirculation. To further investigate the contribution of parenchymal microcirculation to the changes induced by SNP, the time differences between the end point of the SA and the starting point of either the SV or MV compartments were measured. The results showed that the average differences in the RBC appearance time were 0.8 ± 0.4 and 0.9 ± 0.5 s in SA–SV and SA–MV, respectively, under control conditions, and increased to 1.4 ± 0.1 and 1.5 ± 0.2 s following global perturbation. Similarly, the differences in the plasma appearance time were 0.7 ± 0.4 and 0.8 ± 0.5 s for SA–SV and SA–MV, respectively, under control conditions, and increased to 1.2 ± 0.3 and 1.2 ± 0.2 s under global perturbation. These

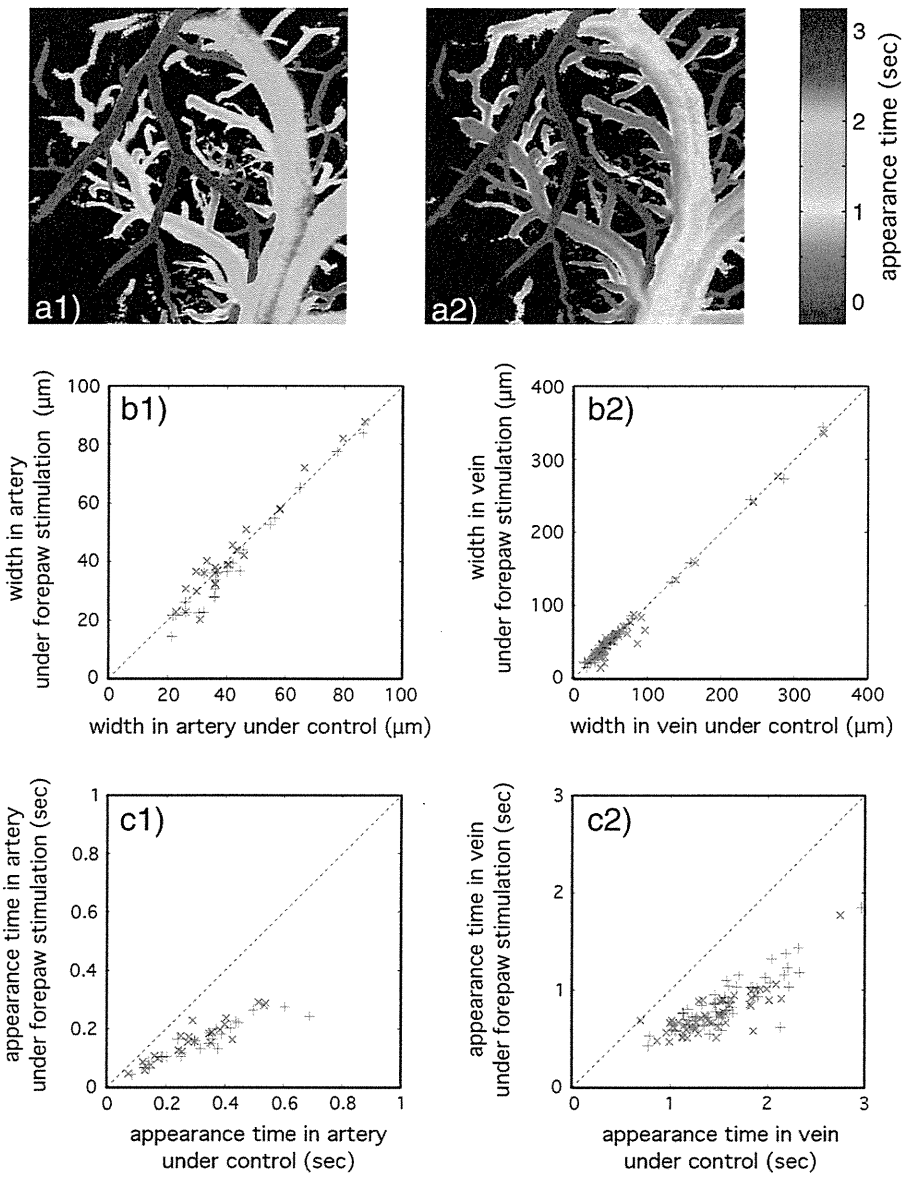

Fig. 4. Representative results for local perturbation measurements (N = 1). (a) Plasma appearance times are shown for control (a1) and forepaw stimulation (a2) conditions. The venous segments showed shortening of appearance time (green/blue to orange/yellow). Changes in vessel width were not evident. (b) Similar widths were maintained for forepaw stimulation in all artery (b1) and venous (b2) segments. The RBC and plasma results are represented as green "+" and red "x", respectively. (c) A comparison of the appearance time measurements. Forepaw stimulation shortened the appearance time slightly in the arteries (c1) and shortened the appearance time greatly in the veins (c2).

results show a large increase in the parenchymal traveling time: there were 0.56 and 0.56 s increases in the RBC appearance times for SA–SV and SA–MV, respectively, and 0.49 and 0.38 s increases in the respective plasma appearance times.

Discussion

To distinguish the vessel type and segments, the present study focused on the spatiotemporal continuity of the fluorescent signal changes measured using high-speed confocal microscopy on a per-pixel basis and across neighboring pixels (Fig. 1), which allowed automatic segmentation without applying spatial filtering (Fig. 2). Because the algorithm relies on the spatial continuity and separability of the fluorescent signal transits within and between the artery and vein compartments, the extension to three-dimensional segmentation can be possible if the signal source originating from the artery and vein components was identified across the different planes. By using a mixed tracer of the fluorescently-labeled RBC and plasma, the present method further allowed cross-image comparisons of the both vessel-by-vessel RBC and plasma passages (Figs. 3 and 4). The demonstrative results showed that the image-based analysis of the flow dynamics provides large numbers of data points for small to large vessels (i.e., about 30 arteries and 55 veins per image, Table 1) and reveals the spatial coherence of the vessel size and type dependent responses (Fig. 5).

Responses to global vs. local perturbation

We observed an identical extension of the RBC and plasma width following the SNP induction (Fig. 5a), which indicates a parallel width shift for RBC and plasma. To confirm this observation, a single-pixel-basis correlation analysis was further performed (Supplemental Fig. S4). The results showed no detectable differences of the RBC and plasma profile changes in the radial directions, i.e. no

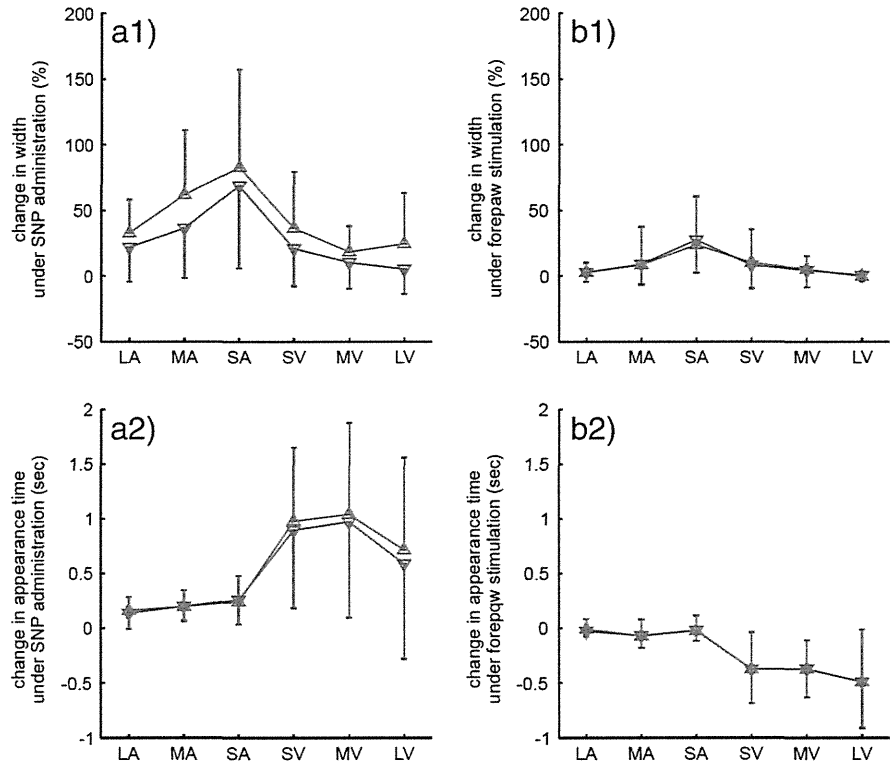

Fig. 5. Width and appearance time changes. The responses to global (a) and local (b) perturbation were compared across all 6 segments; LA: large arteries (>50 μm in a diameter), MA: medium arteries (>25, <50 μm), SA: small arteries (<25 μm), LV: large veins (>100 μm), MV: medium veins (>50, <100 μm), and SV: small veins (<50 μm). The results of the RBC (green) and plasma (red) measurements are indicated as upward-pointing and downward-pointing triangles, respectively. SNP induced vasodilation for all vessels (a1). The largest change was observed for the SA, which was consistent with the forepaw stimulation response (b1). In contrast, different responses to the SNP and forepaw stimulation were seen for the appearance time measurements (a2 and b2). The SNP increased venous appearance time (b2), whereas the forepaw stimulation decreased it. The difference could be related to changes in systemic blood pressure under two conditions. Nevertheless, both conditions provoked the largest gap between SA and SV, which indicate that the changes mostly originate from parenchymal microcirculation. Error bar: standard deviation.

changes in hematocrit level, between control and SNP conditions. The correlation image also showed a thin layer of the intermediate correlation pixels (0.4 to 0.6) near the interface between the vessel and tissue areas. Because the correlation is high (>0.8) in the vessel areas and low (<0.1) in the tissue areas, the lowered correlation indicates dissociation of the RBC and plasma signals (i.e., a plasma layer). The thickness of this layer was measured as 4 to 6 μm, which was slightly larger than the reported size of the plasma layer; 1 to 3 μm in the rat cremaster muscle arteries (Kim et al., 2007), about 3 μm in the rabbit omentum microvessels (Schmid-Schoenbein and Zweifach, 1975), and 4 μm in cat cerebral microvessels (Yamaguchi et al., 1992). The difference between the present and previous reports could be related to the low pixel resolution (3.6 μm/pixel) of our measurements. At the border areas of the vessels, signal to noise ratio tends to be low due to partial volume effects, which may also contribute to the overestimation.

The results of significant vasodilation seen in both arteries and veins under SNP conditions are in good agreement with previous reports (Auer, 1978). On the other hand, local perturbation induced vasodilation in the small arteries, which are also consistent with previous reports (Drew et al., 2011; Vanzetta et al., 2005). The differences in the responses to the two types of perturbation were further revealed in our measurements of the appearance time that showed both an extension and shortening depending on the perturbation. The change of venous appearance time indicates a change of flow speed or traveling distance through parenchymal microcirculation. Because both perturbations induced upstream arterial dilation, the shortening of the traveling distance (i.e., hypoperfusion) is not likely. Thus, the shortened venous appearance time induced by forepaw stimulation indicates an increase in the flow speed (Kleinfeld et al., 1998; Stefanovic et al., 2007), whereas the extended venous appearance time during SNP administration could be due to a decrease in flow speed and/or an increase in the traveling distance. The SNP-induced decrease in the flow speed was further confirmed with correlation analysis of time-intensity curves in two cross-sections (Supplement Fig. S5). Under control conditions, the mean venous speed was 0.89 ± 0.39 and 0.97 ± 0.42 mm/s for the RBC and plasma, respectively ($n = 10$ from one representative animal, Supplemental Fig. S6). Following SNP induction, the mean venous speed decreased to 0.46 ± 0.24 and 0.50 ± 0.29 mm/s for the RBC and plasma, respectively. It should be noted that a slightly faster speed was detected for the plasma in these vessels. This observation contradicts previous reports measured in the cerebral microcirculation (Lin et al., 1995; Rovainen et al., 2003; Schiszler et al., 2000). The contradiction may be due to differences in the vessel size and type investigated. Further improvements of the spatial and temporal resolution for the image acquisition will enable us to provide detailed flow velocity maps, including arterial vessels, in future studies.

Implication for flow regulatory mechanisms in the parenchyma microcirculation

Another important aspect of our observations is that each longitudinal trace appearing in the venous vessel represents a different travel path of the blood through the parenchymal microcirculation. For example, a fast appearance in the venous trace represents a fast path in the parenchymal microcirculation. Considering the

three-dimensional structure of the parenchymal microcirculation (Bär, 1981), it can be expected that a fast path represents a passage through subsurface regions (i.e., a short path), and a slow path represents a passage deep in the parenchyma (i.e., a long path). If the surface arteries primarily respond to cortical activation, the uniform increase in the parenchymal blood flow was expected. However, recent fMRI studies have shown that the earliest vasodilatory response to somatosensory stimulation was evoked at middle cortical layers in the anesthetized rats (Hirano et al., 2011; Tian et al., 2010), suggesting that the parenchymal blood flow was not solely regulated by the cortical surface arteries. Future studies must need to focus on the regulatory mechanism of the parenchymal microcirculation.

Furthermore, the dissociation between the RBC and plasma traces indicates a separation of the RBC and the plasma passages through the parenchymal microcirculation, which may be caused by plasma skimming and/or thoroughfare channels for RBC (Hasegawa et al., 1967; Hudetz et al., 1996; Safaeian et al., 2011). Although no significant differences in the RBC and plasma transit were observed for the appearance times in the present study, the disappearance times showed detectable differences. The average differences in the plasma disappearance times were 1.1 ± 0.5 and 1.6 ± 0.5 s under control conditions for SA–SV and SA–MV, respectively. Both increased by 0.4 s under global perturbation conditions: plasma disappearance times were 1.5 ± 0.9 and 2.0 ± 1.2 s for SA–SV and SA–MV, respectively. On the other hand, average RBC disappearance times were 1.1 ± 0.6 and 1.4 ± 0.6 s for SA–SV and SA–MV, respectively, under control conditions, and 2.1 ± 0.1 and 2.4 ± 0.2 s under global perturbation conditions. As a result, a large increase was seen in the RBC (1.0 s) disappearance time compared with the plasma (0.4 s) disappearance time under global perturbation, which differed from the appearance time results (0.6 and 0.5 s increase in the RBC and plasma appearance times, respectively). In addition, the fact that appearance is sensitive to a fast path, whereas the disappearance is more sensitive to a slow path, indicates that the RBC circulation shifts to the deeper or longer pathways under SNP conditions. These findings clearly show the dissociation of the RBC and plasma passages in the parenchymal microcirculation. With variable perturbations to the model animals, such as neurodegenerative diseases and aging models, future studies will allow further understanding of the role and mechanism of pathway (channel) specific blood flow regulation in the parenchymal microcirculation.

Conclusion

The image-based analytical method for time-lapse images of RBC and plasma dynamics with automatic segmentation was presented. The method enables us to quantify the perturbation-induced changes of the RBC and plasma passages in the individual vessels of the cortical surface and parenchymal microcirculation. Both SNP and forepaw stimuli induced arterial dilation on the cortical surface, whereas the slower and faster transits through the parenchymal microcirculation was observed, depending on the perturbation. The findings support the hypothesis that cortical surface arterial tones and parenchymal blood flow can be individually coordinated.

Supplementary data related to this article can be found online at http://dx.doi.org/10.1016/j.mvr.2012.05.001.

Disclosure

The authors have no conflicts of interest to disclose, and the funding sources had no role on the conduct of the research and preparation of the article.

Contributors

H.K., K.M., and I.K designed the study, K.M. performed experiments, H.K. analyzed data, H.K., K.M., H.I., and I.K. discussed data interpretation, and H.K., K.M., and I.K. wrote the manuscript.

Acknowledgments

This work was partially supported by the Grant-in-Aid for Young Scientists (B) (22700441) (H.K.) and Special Coordination Funds for Promoting Science and Technology (K.M.).

References

Auer, L., 1978. The action of sodium nitroprusside on the pial vessels. Acta Neurochir. (Wien) 43, 297–306.
Autio, J., Kawaguchi, H., Saito, S., Aoki, I., Obata, T., Masamoto, K., Kanno, I., 2011. Spatial frequency-based analysis of mean red blood cell speed in single microvessels: investigation of microvascular perfusion in rat cerebral cortex. PLoS One 6, e24056.
Bär, T., 1981. Distribution of radially penetrating arteries and veins in the neocortex of rat. In: Cervós-Navarro, J., Fritschka, E. (Eds.), Cerebral Microcirculation and Metabolism. Raven Press, New York, pp. 1–8.
Borowsky, I.W., Collins, R.C., 1989. Metabolic anatomy of brain: a comparison of regional capillary density, glucose metabolism, and enzyme activities. J. Comp. Neurol. 288, 401–413.
Drew, P.J., Shih, A.Y., Kleinfeld, D., 2011. Fluctuating and sensory-induced vasodynamics in rodent cortex extend arteriole capacity. Proc. Natl. Acad. Sci. U. S. A. 108, 8473–8478.
Fukuda, M., Wang, P., Moon, C.H., Tanifuji, M., Kim, S.G., 2006. Spatial specificity of the enhanced dip inherently induced by prolonged oxygen consumption in cat visual cortex: implication for columnar resolution functional MRI. NeuroImage 30, 70–87.
Haberl, R.L., Heizer, M.L., Marmarou, A., Ellis, E.F., 1989a. Laser–Doppler assessment of brain microcirculation: effect of systemic alterations. Am. J. Physiol. 256, H1247–H1254.
Haberl, R.L., Heizer, M.L., Ellis, E.F., 1989b. Laser–Doppler assessment of brain microcirculation: effect of local alterations. Am. J. Physiol. 256, H1255–H1260.
Hasegawa, T., Ravens, J.R., Toole, J.F., 1967. Precapillary arteriovenous anastomoses. "Thoroughfare channels" in the brain. Arch. Neurol. 16, 217–224.
Hirano, Y., Stefanovic, B., Silva, A.C., 2011. Spatiotemporal evolution of the functional magnetic resonance imaging response to ultrashort stimuli. J. Neurosci. 31, 1440–1447.
Hudetz, A.G., Fehér, G., Kampine, J.P., 1996. Heterogeneous autoregulation of cerebrocortical capillary flow: evidence for functional thoroughfare channels? Microvasc. Res. 51, 131–136.
Kim, S., Kong, R.L., Popel, A.S., Intaglietta, M., Johnson, P.C., 2007. Temporal and spatial variations of cell-free layer width in arterioles. Am. J. Physiol. Heart Circ. Physiol. 293, H1526–H1535.
Kim, T., Masamoto, K., Fukuda, M., Vazquez, A., Kim, S.G., 2010. Frequency-dependent neural activity, CBF, and BOLD fMRI to somatosensory stimuli in isoflurane-anesthetized rats. NeuroImage 52, 224–233.
Kleinfeld, D., Mitra, P.P., Helmchen, F., Denk, W., 1998. Fluctuations and stimulus-induced changes in blood flow observed in individual capillaries in layers 2 through 4 of rat neocortex. Proc. Natl. Acad. Sci. U. S. A. 95, 15741–15746.
Larson, D.R., Zipfel, W.R., Williams, R.M., Clark, S.W., Bruchez, M.P., Wise, F.W., Webb, W.W., 2003. Water-soluble quantum dots for multiphoton fluorescence imaging in vivo. Science 300, 1434–1436.
Lin, S.Z., Chiou, T.L., Chiang, Y.H., Song, W.S., 1995. Hemodilution accelerates the passage of plasma (not red cells) through cerebral microvessels in rats. Stroke 26, 2166–2171.
Masamoto, K., Kim, T., Fukuda, M., Wang, P., Kim, S.G., 2007. Relationship between neural, vascular, and BOLD signals in isoflurane-anesthetized rat somatosensory cortex. Cereb. Cortex 17, 942–950.
Masamoto, K., Vazquez, A., Wang, P., Kim, S.G., 2008. Trial-by-trial relationship between neural activity, oxygen consumption, and blood flow responses. NeuroImage 40, 442–450.
Mchedlishvili, G., 1986. Chapter 4. Regulation providing an adequate blood supply to cerebral tissue. In: Bevan, J.A. (Ed.), Arterial Behavior and Blood Circulation in the Brain. Plenum Press, New York, pp. 96–175.
Nishimura, N., Schaffer, C.B., Friedman, B., Lyden, P.D., Kleinfeld, D., 2007. Penetrating arterioles are a bottleneck in the perfusion of neocortex. Proc. Natl. Acad. Sci. U. S. A. 104, 365–370.
Park, S.H., Masamoto, K., Hendrich, K., Kanno, I., Kim, S.G., 2008. Imaging brain vasculature with BOLD microscopy: MR detection limits determined by in vivo two-photon microscopy. Magn. Reson. Med. 59, 855–865.
Reniers, D., van Wijk, J., Telea, A., 2008. Computing multiscale curve and surface skeletons of genus 0 shapes using a global importance measure. IEEE Trans. Vis. Comput. Graph. 14, 355–368.
Rosenblum, W.I., Kontos, H.A., 1974. The importance and relevance of studies of the pial microcirculation. Stroke 5, 425–428.
Rovainen, C.M., Woolsey, T.A., Blocher, N.C., Wang, D.B., Robinson, O.F., 2003. Blood flow in single surface arterioles and venules on the mouse somatosensory cortex measured with videomicroscopy, fluorescent dextrans, nonoccluding fluorescent

beads, and computer-assisted image analysis. J. Cereb. Blood Flow Metab. 13, 359–371.
Safaeian, N., Sellier, M., David, T., 2011. A computational model of hemodynamic parameters in cortical capillary networks. J. Theor. Biol. 271, 145–156.
Schaffer, C.B., Friedman, B., Nishimura, N., Schroeder, L.F., Tsai, P.S., Ebner, F.F., Lyden, P.D., Kleinfeld, D., 2006. Two-photon imaging of cortical surface microvessels reveals a robust redistribution in blood flow after vascular occlusion. PLoS Biol. 4, e22.
Schiszler, I., Tomita, M., Fukuuchi, Y., Tanahashi, N., Inoue, K., 2000. New optical method for analyzing cortical blood flow heterogeneity in small animals: validation of the method. Am. J. Physiol. Heart Circ. Physiol. 279, H1291–H1298.
Schmid-Schoenbein, G.W., Zweifach, B.W., 1975. RBC velocity profiles in arterioles and venules of the rabbit omentum. Microvasc. Res. 10, 153–164.
Seylaz, J., Charbonné, R., Nanri, K., Von Euw, D., Borredon, J., Kacem, K., Méric, P., Pinard, E., 1999. Dynamic in vivo measurement of erythrocyte velocity and flow in capillaries and of microvessel diameter in the rat brain by confocal laser microscopy. J. Cereb. Blood Flow Metab. 19, 863–870.
Stefanovic, B., Hutchinson, E., Yakovleva, V., Schram, V., Russell, J.T., Belluscio, L., Koretsky, A.P., Silva, A.C., 2007. Functional reactivity of cerebral capillaries. J. Cereb. Blood Flow Metab. 28, 961–972.
Tian, P., Teng, I.C., May, L.D., Kurz, R., Lu, K., Scadeng, M., Hillman, E.M., De Crespigny, A.J., D'Arceuil, H.E., Mandeville, J.B., Marota, J.J., Rosen, B.R., Liu, T.T., Boas, D.A., Buxton, R.B., Dale, A.M., Devor, A., 2010. Cortical depth-specific microvascular dilation underlies laminar differences in blood oxygenation level-dependent functional MRI signal. Proc. Natl. Acad. Sci. U. S. A. 107, 15246–15251.
Vanzetta, I., Hildesheim, R., Grinvald, A., 2005. Compartment-resolved imaging of activity-dependent dynamics of cortical blood volume and oximetry. J. Neurosci. 25, 2233–2244.
Yamaguchi, S., Yamakawa, T., Niimi, H., 1992. Cell-free plasma layer in cerebral microvessels. Biorheology 29, 251–260.